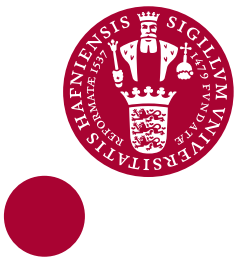

In vivo assessment of optical properties of basal cell carcinoma and differentiation of BCC subtypes by high-definition optical coherence tomography

Boone, Marc; Suppa, Mariano; Miyamoto, Makiko; Marneffe, Alice; Jemec, Gregor; Del Marmol, Véronique

Published in:
Biomedical Optics Express

DOI:
10.1364/BOE.7.002269

Publication date:
2016

Document version
Publisher's PDF, also known as Version of record

Document license:
Unspecified

Citation for published version (APA):
Boone, M., Suppa, M., Miyamoto, M., Marneffe, A., Jemec, G., & Del Marmol, V. (2016). *In vivo* assessment of optical properties of basal cell carcinoma and differentiation of BCC subtypes by high-definition optical coherence tomography. *Biomedical Optics Express*, *7*(6), 2269-2284. https://doi.org/10.1364/BOE.7.002269

Biomedical Optics EXPRESS

In vivo assessment of optical properties of basal cell carcinoma and differentiation of BCC subtypes by high-definition optical coherence tomography

Marc Boone,[1,*] Mariano Suppa,[1] Makiko Miyamoto,[1] Alice Marneffe,[1] Gregor Jemec,[2] and Veronique Del Marmol[1]

[1]*Department of Dermatology, Université Libre de Bruxelles, Hôpital Erasme, Belgium*
[2]*Department of Dermatology, Roskilde Hospital, University of Copenhagen, Denmark*
[*]*dr.boone@scarlet.be*

Abstract: High-definition optical coherence tomography (HD-OCT) features of basal cell carcinoma (BCC) have recently been defined. We assessed in vivo optical properties (IV-OP) of BCC, by HD-OCT. Moreover their critical values for BCC subtype differentiation were determined. The technique of semi-log plot whereby an exponential function becomes linear has been implemented on HD-OCT signals. The relative attenuation factor (μ_{raf}) at different skin layers could be assessed. IV-OP of superficial BCC with high diagnostic accuracy (DA) and high negative predictive values (NPV) were (i) decreased μ_{raf} in lower part of epidermis and (ii) increased epidermal thickness (E-T). IV-OP of nodular BCC with good to high DA and NPV were (i) less negative μ_{raf} in papillary dermis compared to normal adjacent skin and (ii) significantly decreased E-T and papillary dermal thickness (PD-T). In infiltrative BCC (i) high μ_{raf} in reticular dermis compared to normal adjacent skin and (ii) presence of peaks and falls in reticular dermis had good DA and high NPV. HD-OCT seems to enable the combination of in vivo morphological analysis of cellular and 3-D micro-architectural structures with IV-OP analysis of BCC. This permits BCC sub-differentiation with higher accuracy than in vivo HD-OCT analysis of morphology alone.

OCIS codes: (170.4500) Optical coherence tomography; (170.1870) Dermatology; (170.3660) Light propagation in tissues; (170.6935) Tissue characterization; (170.7050) Turbid media; (290.0290) Scattering.

References and links

1. S. C. Flohil, E. de Vries, H. A. Neumann, J. W. Coebergh, and T. Nijsten, "Incidence, prevalence and future trends of primary basal cell carcinoma in the Netherlands," Acta Derm. Venereol. **91**(1), 24–30 (2011).
2. J. Roewert-Huber, B. Lange-Asschenfeldt, E. Stockfleth, and H. Kerl, "Epidemiology and aetiology of basal cell carcinoma," Br. J. Dermatol. **157**(Suppl 2), 47–51 (2007).
3. A. E. Carsin, L. Sharp, and H. Comber, "Geographical, urban/rural and socioeconomic variations in nonmelanoma skin cancer incidence: a population-based study in Ireland," Br. J. Dermatol. **164**(4), 822–829 (2011).
4. K. Sellheyer, "Basal cell carcinoma: cell of origin, cancer stem cell hypothesis and stem cell markers," Br. J. Dermatol. **164**(4), 696–711 (2011).
5. M. Trakatelli, C. Morton, E. Nagore, C. Ulrich, V. Del Marmol, K. Peris, N. Basset-Seguin, and BCC subcommittee of the Guidelines Committee of the European Dermatology Forum, "Update of the European guidelines for basal cell carcinoma management," Eur. J. Dermatol. **24**(3), 312–329 (2014).
6. A. H. Arits, K. Mosterd, B. A. Essers, E. Spoorenberg, A. Sommer, M. J. De Rooij, H. P. van Pelt, P. J. Quaedvlieg, G. A. Krekels, P. A. van Neer, J. J. Rijzewijk, A. J. van Geest, P. M. Steijlen, P. J. Nelemans, and N. W. Kelleners-Smeets, "Photodynamic therapy versus topical imiquimod versus topical fluorouracil for

#260406 Received 2 Mar 2016; revised 15 May 2016; accepted 15 May 2016; published 19 May 2016

treatment of superficial basal-cell carcinoma: a single blind, non-inferiority, randomised controlled trial," Lancet Oncol. **14**(7), 647–654 (2013).
7. A. H. Arits, M. H. Schlangen, P. J. Nelemans, and N. W. Kelleners-Smeets, "Trends in the incidence of basal cell carcinoma by histopathological subtype," J. Eur. Acad. Dermatol. Venereol. **25**(5), 565–569 (2011).
8. C. A. Banzhaf, L. Themstrup, H. C. Ring, M. Mogensen, and G. B. Jemec, "Optical coherence tomography imaging of non-melanoma skin cancer undergoing imiquimod therapy," Skin Res. Technol. **20**(2), 170–176 (2014).
9. L. Themstrup, C. A. Banzhaf, M. Mogensen, and G. B. Jemec, "Optical coherence tomography imaging of non-melanoma skin cancer undergoing photodynamic therapy reveals subclinical residual lesions," Photodiagn. Photodyn. Ther. **11**(1), 7–12 (2014).
10. D. Altamura, S. W. Menzies, G. Argenziano, I. Zalaudek, H. P. Soyer, F. Sera, M. Avramidis, K. DeAmbrosis, M. C. Fargnoli, and K. Peris, "Dermatoscopy of basal cell carcinoma: morphologic variability of global and local features and accuracy of diagnosis," J. Am. Acad. Dermatol. **62**(1), 67–75 (2010).
11. J. Giacomel and I. Zalaudek, "Pink lesions," Dermatol. Clin. **31**(4), 649–678 (2013).
12. A. Gulia, D. Altamura, S. De Trane, T. Micantonio, M. C. Fargnoli, and K. Peris, "Pigmented reticular structures in basal cell carcinoma and collision tumours," Br. J. Dermatol. **162**(2), 442–444 (2010).
13. A. Lallas, T. Tzellos, A. Kyrgidis, Z. Apalla, I. Zalaudek, A. Karatolias, G. Ferrara, S. Piana, C. Longo, E. Moscarella, A. Stratigos, and G. Argenziano, "Accuracy of dermoscopic criteria for discriminating superficial from other subtypes of basal cell carcinoma," J. Am. Acad. Dermatol. **70**(2), 303–311 (2014).
14. T. Micantonio, A. Gulia, E. Altobelli, A. Di Cesare, R. Fidanza, A. Riitano, M. C. Fargnoli, and K. Peris, "Vascular patterns in basal cell carcinoma," J. Eur. Acad. Dermatol. Venereol. **25**(3), 358–361 (2011).
15. M. Suppa, T. Micantonio, A. Di Stefani, H. P. Soyer, S. Chimenti, M. C. Fargnoli, and K. Peris, "Dermoscopic variability of basal cell carcinoma according to clinical type and anatomic location," J. Eur. Acad. Dermatol. Venereol. **29**(9), 1732–1741 (2015).
16. A. L. Agero, K. J. Busam, C. Benvenuto-Andrade, A. Scope, M. Gill, A. A. Marghoob, S. González, and A. C. Halpern, "Reflectance confocal microscopy of pigmented basal cell carcinoma," J. Am. Acad. Dermatol. **54**(4), 638–643 (2006).
17. R. P. Castro, A. Stephens, N. A. Fraga-Braghiroli, M. C. Oliviero, G. G. Rezze, H. Rabinovitz, and A. Scope, "Accuracy of in vivo confocal microscopy for diagnosis of basal cell carcinoma: a comparative study between handheld and wide-probe confocal imaging," J. Eur. Acad. Dermatol. Venereol. **29**(6), 1164–1169 (2015).
18. S. González and Z. Tannous, "Real-time, in vivo confocal reflectance microscopy of basal cell carcinoma," J. Am. Acad. Dermatol. **47**(6), 869–874 (2002).
19. P. Guitera, S. W. Menzies, C. Longo, A. M. Cesinaro, R. A. Scolyer, and G. Pellacani, "In vivo confocal microscopy for diagnosis of melanoma and basal cell carcinoma using a two-step method: analysis of 710 consecutive clinically equivocal cases," J. Invest. Dermatol. **132**(10), 2386–2394 (2012).
20. C. Longo, A. Lallas, A. Kyrgidis, H. Rabinovitz, E. Moscarella, S. Ciardo, I. Zalaudek, M. Oliviero, A. Losi, S. Gonzalez, P. Guitera, S. Piana, G. Argenziano, and G. Pellacani, "Classifying distinct basal cell carcinoma subtype by means of dermatoscopy and reflectance confocal microscopy," J. Am. Acad. Dermatol. **71**(4), 716–724 (2014).
21. S. Nori, F. Rius-Díaz, J. Cuevas, M. Goldgeier, P. Jaen, A. Torres, and S. González, "Sensitivity and specificity of reflectance-mode confocal microscopy for in vivo diagnosis of basal cell carcinoma: a multicenter study," J. Am. Acad. Dermatol. **51**(6), 923–930 (2004).
22. T. Gambichler, A. Orlikov, R. Vasa, G. Moussa, K. Hoffmann, M. Stücker, P. Altmeyer, and F. G. Bechara, "In vivo optical coherence tomography of basal cell carcinoma," J. Dermatol. Sci. **45**(3), 167–173 (2007).
23. M. Mogensen and G. B. Jemec, "Diagnosis of nonmelanoma skin cancer/keratinocyte carcinoma: a review of diagnostic accuracy of nonmelanoma skin cancer diagnostic tests and technologies," Dermatol. Surg. **33**(10), 1158–1174 (2007).
24. M. Mogensen, T. M. Joergensen, B. M. Nürnberg, H. A. Morsy, J. B. Thomsen, L. Thrane, and G. B. Jemec, "Assessment of optical coherence tomography imaging in the diagnosis of non-melanoma skin cancer and benign lesions versus normal skin: observer-blinded evaluation by dermatologists and pathologists," Dermatol. Surg. **35**(6), 965–972 (2009).
25. M. Mogensen, B. M. Nürnberg, J. L. Forman, J. B. Thomsen, L. Thrane, and G. B. Jemec, "In vivo thickness measurement of basal cell carcinoma and actinic keratosis with optical coherence tomography and 20-MHz ultrasound," Br. J. Dermatol. **160**(5), 1026–1033 (2009).
26. J. M. Olmedo, K. E. Warschaw, J. M. Schmitt, and D. L. Swanson, "Optical coherence tomography for the characterization of basal cell carcinoma in vivo: a pilot study," J. Am. Acad. Dermatol. **55**(3), 408–412 (2006).
27. M. Ulrich, T. von Braunmuehl, H. Kurzen, T. Dirschka, C. Kellner, E. Sattler, C. Berking, J. Welzel, and U. Reinhold, "The sensitivity and specificity of optical coherence tomography for the assisted diagnosis of nonpigmented basal cell carcinoma: an observational study," Br. J. Dermatol. **173**(2), 428–435 (2015).
28. S. Seidenari, F. Arginelli, S. Bassoli, J. Cautela, A. M. Cesinaro, M. Guanti, D. Guardoli, C. Magnoni, M. Manfredini, G. Ponti, and K. König, "Diagnosis of BCC by multiphoton laser tomography," Skin Res. Technol. **19**(1), e297–e304 (2013).
29. T. Gambichler, I. Plura, P. Kampilafkos, K. Valavanis, M. Sand, F. G. Bechara, and M. Stücker, "Histopathological correlates of basal cell carcinoma in the slice and en face imaging modes of high-definition optical coherence tomography," Br. J. Dermatol. **170**(6), 1358–1361 (2014).

#260406 Received 2 Mar 2016; revised 15 May 2016; accepted 15 May 2016; published 19 May 2016

30. T. Maier, D. Kulichová, T. Ruzicka, C. Kunte, and C. Berking, "Ex vivo high-definition optical coherence tomography of basal cell carcinoma compared to frozen-section histology in micrographic surgery: a pilot study," J. Eur. Acad. Dermatol. Venereol. **28**(1), 80–85 (2014).
31. M. A. Boone, S. Norrenberg, G. B. Jemec, and V. Del Marmol, "Imaging of basal cell carcinoma by high-definition optical coherence tomography: histomorphological correlation. A pilot study," Br. J. Dermatol. **167**(4), 856–864 (2012).
32. T. Maier, M. Braun-Falco, T. Hinz, M. H. Schmid-Wendtner, T. Ruzicka, and C. Berking, "Morphology of basal cell carcinoma in high definition optical coherence tomography: en-face and slice imaging mode, and comparison with histology," J. Eur. Acad. Dermatol. Venereol. **27**(1), e97–e104 (2013).
33. M. A. Boone, M. Suppa, G. Pellacani, A. Marneffe, M. Miyamoto, I. Alarcon, C. Ruini, R. Hofmann-Wellenhof, J. Malvehy, G. B. Jemec, and V. Del Marmol, "High-definition optical coherence tomography algorithm for discrimination of basal cell carcinoma from clinical BCC imitators and differentiation between common subtypes," J. Eur. Acad. Dermatol. Venereol. **29**(9), 1771–1780 (2015).
34. M. Suppa, G. Forchetti, M. Miyamoto, A. Marneffe, T. Seremet, V. Del Marmol, and M. Boone, "Validation of a new algorithm for basal cell carcinoma diagnosis and subtype classification by means of high-definition optical coherence tomography," Br. J. Dermatol. submitted.
35. C. Herman, "Emerging technologies for the detection of melanoma: achieving better outcomes," Clin. Cosmet. Investig. Dermatol. **5**, 195–212 (2012).
36. O. Ibrahim, B. Gastman, and A. Zhang, "Advances in diagnosis and treatment of nonmelanoma skin cancer," Ann. Plast. Surg. **73**(5), 615–619 (2014).
37. R. J. Marshall, "Infrared and ultraviolet photography in a study of the selective absorption of radiation by pigmented lesions of skin," Med. Biol. Illus. **26**(2), 71–84 (1976).
38. M. A. Boone, M. Suppa, A. Marneffe, M. Miyamoto, G. B. Jemec, and V. Del Marmol, "High-definition optical coherence tomography intrinsic skin ageing assessment in women: a pilot study," Arch. Dermatol. Res. **307**(8), 705–720 (2015).
39. M. A. Boone, M. Suppa, F. Dhaenens, M. Miyamoto, A. Marneffe, G. B. Jemec, V. Del Marmol, and R. Nebosis, "In vivo assessment of optical properties of melanocytic skin lesions and differentiation of melanoma from non-malignant lesions by high-definition optical coherence tomography," Arch. Dermatol. Res. **308**(1), 7–20 (2016), doi:10.1007/s00403-015-1608-5.
40. M. Boone, G. B. Jemec, and V. Del Marmol, "High-definition optical coherence tomography enables visualization of individual cells in healthy skin: comparison to reflectance confocal microscopy," Exp. Dermatol. **21**(10), 740–744 (2012).
41. M. A. Boone, S. Norrenberg, G. B. Jemec, and V. Del Marmol, "High-definition optical coherence tomography imaging of melanocytic lesions: a pilot study," Arch. Dermatol. Res. **306**(1), 11–26 (2014).
42. V. V. Tuchin, "Tissue and blood optical immersion by exogenous chemical agents," in *Optical clearing of tissues and blood*, V. V. Tuchin, ed. (SPIE - The international Society for Optical Engineering, 2006), pp. 1 - 19.
43. S. L. Jacques, "Fractal nature of light scattering in tissues," J. Innov. Opt. Health Sci. **4**(01), 1–7 (2011).
44. S. L. Jacques, "Optical properties of biological tissues: a review," Phys. Med. Biol. **58**(11), R37–R61 (2013).
45. S. Jacques, R. Samatham, N. Choudhury, Y. Fu, and D. Levitz, "Measuring tissue optical properties in vivo using reflectance-mode confocal microscopy and optical coherence tomography," Proc. SPIE **6864**, 68640B (2008).
46. L. A. Sordillo, Y. Pu, S. Pratavieira, Y. Budansky, and R. R. Alfano, "Deep optical imaging of tissue using the second and third near-infrared spectral windows," J. Biomed. Opt. **19**(5), 056004 (2014).
47. S. L. Jacques and B. W. Pogue, "Tutorial on diffuse light transport," J. Biomed. Opt. **13**(4), 041302 (2008).
48. T. Lister, P. A. Wright, and P. H. Chappell, "Optical properties of human skin," J. Biomed. Opt. **17**(9), 0909011 (2012).
49. V. V. Tuchin, I. L. Maksimova, D. A. Zimnyakov, I. L. Kon, A. H. Mavlyutov, and A. A. Mishin, "Light propagation in tissues with controlled optical properties," J. Biomed. Opt. **2**(4), 401–417 (1997).
50. A. P. Ivanov, S. A. Makarevich, and A. Y. Khairulina, "Propagation of radiation in tissues and liquids with densily packed scatterers," J. Appl. Spectrosc. **47**, 7 (1988).
51. S. Neerken, G. W. Lucassen, M. A. Bisschop, E. Lenderink, and T. A. Nuijs, "Characterization of age-related effects in human skin: A comparative study that applies confocal laser scanning microscopy and optical coherence tomography," J. Biomed. Opt. **9**(2), 274–281 (2004).
52. I. L. Shlivko, M. Y. Kirillin, E. V. Donchenko, D. O. Ellinsky, O. E. Garanina, M. S. Neznakhina, P. D. Agrba, and V. A. Kamensky, "Identification of layers in optical coherence tomography of skin: comparative analysis of experimental and Monte Carlo simulated images," Skin Res. Technol. **21**(4), 419–425 (2015).
53. G. Zonios, A. Dimou, M. Carrara, and R. Marchesini, "In vivo optical properties of melanocytic skin lesions: common nevi, dysplastic nevi and malignant melanoma," Photochem. Photobiol. **86**(1), 236–240 (2010).
54. E. Salomatina, B. Jiang, J. Novak, and A. N. Yaroslavsky, "Optical properties of normal and cancerous human skin in the visible and near-infrared spectral range," J. Biomed. Opt. **11**(6), 064026 (2006).
55. U. Baran, Y. Li, and R. K. Wang, "In vivo tissue injury mapping using optical coherence tomography based methods," Appl. Opt. **54**(21), 6448–6453 (2015).

#260406 Received 2 Mar 2016; revised 15 May 2016; accepted 15 May 2016; published 19 May 2016

1. Introduction

Basal cell carcinoma (BCC) is the most prevalent skin cancer among Caucasians [1,2]. The incidence of BCC continues to increase worldwide. As a consequence, BCC treatment is associated with relevant health costs for the society. It is a multifactorial disease in which excessive sun exposure plays a major pathogenic role [3,4].

Treatment strategy has changed in the last two decades [5]. With the emergence of non-invasive therapies for superficial BCC (sBCC) such as topical immunotherapies and photodynamic therapy, there is an urgent demand for real time non-invasive diagnosis and monitoring [6–9].

Nowadays, a broad variety of imaging techniques are becoming available. Dermoscopy is very useful for the clinical diagnosis of BCC [10–15]. In the past decade other non-invasive techniques including reflectance confocal microscopy (RCM) [16–21], conventional optical coherence tomography (C-OCT) [22–27] and multiphoton tomography (MPT) [28] have become available for the in-vivo diagnosis of BCC. Of these, RCM in the hands of an expert has shown high diagnostic accuracy for the diagnosis of BCC, with a sensitivity of 100% and a specificity of 85% in a large multicenter study [19]. The diagnostic accuracy of MPT still needs to be determined [28]. The diagnostic accuracy of C-OCT has been evaluated in large multicenter studies [25–28].

High-definition optical coherence tomography (HD-OCT) is a recently introduced non-invasive real-time 3-D imaging technique with cellular resolution, which may aid in BCC diagnosis and managing [29–32]. Based on 3-D HD-OCT features of BCC a diagnostic algorithm is proposed permitting discrimination of BCC from clinical BCC imitators and differentiation of BCC subtypes [33]. Additionally, a testing set has been performed [34] to assess the diagnostic performance of this algorithm. The diagnostic accuracy of each observer was clearly associated with the level of experience, which suggests the existence of a learning curve.

New diagnostic tools providing automated classification of skin lesions usable by non-experts, have been proposed [35,36]. Spectral methods fall into this class of emerging new techniques holding the promise to improve early diagnosis of skin cancer [36,37]. In two recent studies we demonstrated that HD-OCT permits to quantify in vivo optical properties (IV-OP) such as light attenuation in intrinsic ageing skin [38] and in melanocytic lesions [39]. This approach seems to permit a semi-automated classification of skin lesions easier to handle by non-experts.

Therefore the aim of this paper was to quantify IV-OP of BCC, such as light attenuation, by means of HD-OCT in comparison with normal adjacent skin. An additional objective was to determine the best critical value of these optical properties for BCC subtype discrimination.

2. Methods

2.1 Study sample

This retrospective pilot study included HD-OCT images of sBCC, nodular BCC (nBCC) and infiltrative BCC (iBCC) consecutively retrieved at first author's private practice between January 2011 and November 2015. HD-OCT images of the healthy skin adjacent to each BCC were also taken and used as control. Inclusion criteria were: (i) confirmed histopathological diagnosis of BCC subtype and (ii) availability of good quality HD-OCT images.

All patients provided informed consent for imaging their lesion by HD-OCT (Skintell, Agfa Healthcare, Mortsel, Belgium). We conformed to the Helsinki Declaration with respect to human subjects in biomedical research. All international rules governing clinical investigation of human subjects were strictly followed. Approval from local ethical

#260406 Received 2 Mar 2016; revised 15 May 2016; accepted 15 May 2016; published 19 May 2016

committee was obtained (P2015-389). Moreover this study affected neither the routine diagnosis nor treatment of the lesions presented by the included subjects.

2.2 Histopathology

In the present study, all lesions were fully excised and examined histopathologically for diagnostic confirmation. Histopathological analysis was carried out by two board-certified histopathologists.

2.3 Image acquisition by HD-OCT

Instruments and acquisition methods and technical details have been previously described [40–42]. For the purpose of this study we will remind that HD-OCT offers a constant homogeneous resolution of 3 µm in all three dimensions. The system is capable of capturing a cross-sectional and en face image in real time, with a fast real time 3-D acquisition. A sharp image at all depth is guaranteed up to a depth of 570 µm. The field of view is 1.8 x 1.5 mm. The total light power at the tissue is < 3.5 mW.

2.4 HD-OCT focus tracking permits IV-OP analysis

Skin is a highly turbid medium. Light that propagates through skin is scattered and absorbed resulting in its attenuation. In contradiction to a "normal" light detector, HD-OCT only detects photons which reach the detector on an almost straight path – the ballistic portion of the photons or photons which were only forward scattered a few times [43].

Table 1. Parameters (abbreviation and definition) used in this study

Abbreviation	Definition
SE-S	Skin entrance (SE) signal. OCT signal (arbitrary unit, a.u.) at SE. Corresponds to the first bright band (first peak: FP) on cross-sectional imaging (Fig. 1).
DEJ-S	Dermo-epidermal junction (DEJ) signal. OCT signal (a.u.) at DEJ. DEJ corresponds to a dark band under the epidermis (valley: V) on cross-sectional imaging (Fig. 1).
PRDJ-S	Papillary-reticular dermis junction (PRDJ) signal. OCT signal (a.u.) at PRDJ. Corresponds to the second peak (SP) after the valley (Fig. 1).
Layer-1	Epidermal layer: from SE (first peak) to DEJ (valley)
Layer-2	Papillary dermal layer: from DEJ (valley) to PRDJ (second peak)
Layer-3	Superficial reticular dermal layer: from PRDJ up to a depth of 570µm (theoretical penetration depth of HD-OCT).
E-T	Difference (µm) in Z-values (depth) between FP and V. This corresponds approximately to the epidermal thickness (E-T) if DEJ is very thin [38]
PD-T	Difference (µm) in Z-values (depth) between V and SP. This corresponds approximately to the papillary dermis thickness (PD-T) if DEJ is very thin [38].
Nod	Corresponds to a specific Z-value within a layer where the slope of the curve changes, dividing the layer into two sublayers.
Nod-L1	Presence of nod in semi-log plot in layer-1 dividing the epidermis in upper part (1a) and deeper part (1b). If the epidermal thickness of a BCC is lesser than the thickness of corresponding normal adjacent epidermis, absence of Nod-L1 will be assumed.
Nod-L3	Presence of nod in semi-log plot in layer-3 dividing the superficial reticular dermis in upper part (3a) and deeper part (3b).
P&F-L3 (numerical variable = $\sum$ per lesion)	This corresponds to the number of small increases of backscattering (peak) immediately followed by a decrease of backscattering (fall), disturbing the semi-log plot in layer 3, count up in a single BCC lesion or adjacent normal skin.
P&F-L3$_{am}$ (mean = $\sum$ ($\sum$ per lesion)/16)	The arithmetic mean of P&F-L3 is calculated by adding up all numbers of P&Fs in a set of BCC subtypes or corresponding adjacent skin and dividing this sum by the number of BCC lesions (#16) or normal adjacent skin (#16) in that set.
$\mu_{raf1\text{-}3}$	Relative attenuation factor (μm^{-1}). The calculated attenuation coefficients are not absolute. The SE-S is used as reference intensity. Hence "relative" refers to the attenuation coefficient normalized to skin entrance signal for each of the three layers. Negative values for μ_{raf} imply increased backscattering.
μ_{raf1a}, μ_{raf1b}	A nod is present in layer-1 dividing μ_{raf1} in μ_{raf1a} (part above nod) and μ_{raf1b} (part under nod). If Nod-L1 is absent μ_{raf1} is divided in μ_{raf1a} (μ_{raf1} in upper ½ of the epidermis) and μ_{raf1b} (μ_{raf1} in lower ½ of epidermal layer).
μ_{raf3a}, μ_{raf3b}	A nod is present in layer-3 dividing μ_{raf3} in an upper part μ_{raf3a} and a deeper part μ_{raf3b}.

#260406 Received 2 Mar 2016; revised 15 May 2016; accepted 15 May 2016; published 19 May 2016

The resulting attenuation coefficient was estimated by Jacques and associates [44–46]. Since absorption is much smaller than scattering for tissues in the near infrared (NIR) spectrum, absorption can be neglected [47]. HD-OCT operates in the second diagnostic window of the NIR spectrum [38,39] and hence the main attenuation mechanism for HD-OCT is scattering. Measuring tissue optical properties in vivo is only applicable to OCT when operating in focus-tracking mode which is the case for HD-OCT [44]. A table providing definitions and abbreviations of optical properties adapted from the literature [43–51] and relevant for this manuscript was already published [39].

2.5 In vivo optically probing and relative attenuation factor

The decay of reflectance (backscattered intensity) with imaging depth of ballistic photons is a process that can be well-modelled by an exponential relationship [44,50]. When operating in the NIR diagnostic window, absorption becomes negligible and the slope of the exponential attenuation is proportional to the reduced scattering coefficient μ'_s [44,50]. Analysis of the exponential profile of light attenuation by semi-log plot (an exponential function becomes a straight line given by $y = ax + b$), can provide information on tissue scattering properties [44,50].

The procedure used in this study is illustrated in Fig. 1. A 3-D HD-OCT DICOM (digital imaging and communication in medicine) image of the lesion was selected. This DICOM file was then opened using LabView software. A rectangular region of interest (> 0.1 mm^2) was chosen in the en face image in order to i) obtain a clear-cut sample of the lobular structures, ii) avoid mismatching between layers (if skin surface was obliquely with respect to the probe), and iii) exclude "artefacts" (wrinkles, follicles) from the sample. A plot z-axis profile of this region was performed. The obtained graph displayed the reflectance and attenuation of the ballistic photons (OCT-signal) which was measured on the y-axis with arbitral units (a.u.) versus imaging depth which is indicated on the x-axis (μm). The first peak corresponded with the skin entrance signal (SE-S). The distance from Z = 0 to the first peak was the thickness of the optical gel.

In order to normalize the OCT signal, the offset corresponding with the mean signal within optical gel were removed from each OCT signal in a first step. In a second step, all these HD-OCT values were divided by SE-S in order to normalize them to the SE-S (see graph a3 in Figs. 1, 2, and 3). To measure the absolute attenuation coefficient it is necessary to have a measurement system with a perfectly linear behaviour. The numerical measurement values must be proportional to the light intensity. This calibration was not tested to the full extent with the Skintell. Hence, the SE-S was used as reference intensity as this signal is clearly defined. Moreover, absolute values of attenuation are not required as only differences in attenuation were taken into account. The natural logarithm ln(x) of those normalized values was taken (see graph a4 in Figs. 1, 2, and 3). An exponential function became linear described by $y = ax + b$ (Semi-log plot) whereby coefficient a provided the relative attenuation factor μ_{raf}, which is the attenuation coefficient normalized to the SE-S.

2.6 The following optical properties were measured (see Table 1 for abbreviations)

The following OCT signals were measured at different selected Z-values: SE-S, DEJ-S, PRDJ-S (arbitrary unit, a.u.). The junction between PD and RD (PRDJ) is represented by the highest peak after the valley [38,51]. The thickness (μm) of epidermis and papillary dermis were calculated. Successive layers with clear exponential decay were identified and plotted: epidermis (layer-1), papillary dermis (layer-2) and superficial papillary dermis (layer-3). A straight line was fitted in each of the three layers (i = 1 to3) resulting in equation of the type $y_i = a_i x_i + b_i$ whereby coefficient a provided the relative attenuation factor for each of the three layers ($\mu_{raf1\text{-}3}$; μm^{-1}). The presence/absence of nods in semi-log plot (Nod-L1 and Nod-

#260406 Received 2 Mar 2016; revised 15 May 2016; accepted 15 May 2016; published 19 May 2016

L3) were identified (Yes/No). Supplementary peaks and falls in third layer (P&F-L3) were evaluated.

If a nod was present in layer-1, the relative attenuation factor μ_{raf1} was subdivided in μ_{raf1a} and μ_{raf1b}. If Nod-L1 was absent μ_{raf1} was divided in μ_{raf1a} (μ_{raf1} in upper ½ of the epidermis) and μ_{raf1b} (μ_{raf1} in lower ½ of epidermal layer). Negative values for μ_{raf} imply increased backscattering.

2.7 Statistical analysis

The paired T-test was used to compare lesioned to healthy adjacent skin. The unpaired (two-sample) T-test was used to compare normal adjacent skin of the three BCC subtypes (NL-sBCC, NL-nBCC and NL-iBCC).

One-way analysis of variance (ANOVA) was used to compare means of three samples (sBCC, nBCC, iBCC) using the F distribution. Prior to the Anova test, Levene's Test for "equality of variances" was performed. If the Levene test was positive ($P<0.05$) then the variances in the different groups were different (the groups are not homogeneous) and a logarithmic transformation to the data has been performed. Moreover Scheffé test was used for all pairwise comparisons.

The best critical value of all HD-OCT assessed optical properties was determined by applying the receiver operating characteristic (ROC) curves. This is a graph displaying the relationship between the true positive rate (on the vertical axis) and the false positive rate (on the horizontal axis).

Based on these critical values absolute and relative frequencies were calculated for the three subgroups. Chi-squared (X^2) test was employed to compare subgroups. The phi (φ) coefficient, employed to weight diagnostic power of each significant parameter, is a measure of association of two binary variables and is related to the chi-squared (X^2) statistic by the formula: $\varphi^2 = X^2/n$, where n equals the total number of observations. Calculations were made by using MedCalc statistical software version 14.12.0.

3. Results

3.1 Subjects

We included in this study 48 cases comprising 16 sBCC, 16 nBCC and 16 iBCC. All sBCC were located on the trunk. All nBCC and iBCC were located on the face, except for 1 nBCC and 2 iBCC with truncal localization. The study lesions belonged to 28 females and 20 males with skin type I-III and ages ranging from 45 to 84 years (median 61 years). The healthy skin adjacent to each of the 48 included BCC was also imaged (16 NL-sBCC, 16 NL-nBCC and 16 NL-iBCC).

3.2 Quantitative IV-OP analysis (Table 2)

3.2.1 Comparison between trunk and facial skin. NL-sBCC (predominantly trunk) versus NL-nBCC and NL-iBCC (predominantly face) (p-values in columns 3, 6 and 9 respectively)

Normal skin adjacent to sBCC (NL-sBCC) presented significant differences ($p<0.01$) regarding SE-S, PRDJ-S, E-T, PD-T, μ_{raf1a}, μ_{raf2}, μ_{raf3a}, μ_{raf3b} in comparison with normal skin adjacent to nBCC (NL-nBCC) and iBCC (NL-iBCC). No significant differences were observed between NL-nBCC and NL-iBCC except for μ_{raf3b}. A significant difference ($p<0.01$) regarding μ_{raf3b} was observed between the three subgroups.

3.2.2 Comparison between BCC subtype (sBCC, nBCC and iBCC) and corresponding normal adjacent skin (p-values in columns 4,7 and 10 respectively)

Compared to NL-sBCC, sBCC presented significant differences ($p<0.001$) regarding SE-S, DEJ-S, PRDJ-S, E-T, μ_{raf1b}. Compared to NL-nBCC, nBCC presented significant differences

#260406 Received 2 Mar 2016; revised 15 May 2016; accepted 15 May 2016; published 19 May 2016

($p<0.001$) regarding E-T and PD-T. Moreover in nBCC no NOD-L1, higher P&F-L3, lower μ_{raf1a}, higher μ_{raf1b} were detected ($p<0.01$) compared to NL-nBCC. A less negative μ_{raf2} compared to NL-nBCC was only ($p<0.01$) observed in nBCC. Compared to NL-iBCC, iBCC presented significant differences ($p<0.01$) regarding DEJ-S, PRDJ-S, E-T and PD-T. Moreover compared to NL-iBCC, iBCC presented no NOD-L1, higher P&F-L3, lower μ_{raf1a} and higher μ_{raf1b}. A significant increase ($p<0.01$) of μ_{raf3b} compared to normal adjacent skin was only observed in iBCC and not in the other BCC subgroups.

3.2.3 Comparison between BCC subtypes (Figs. 1, 2, and 3) (p-values in columns 2, 5 and 8 respectively)

No significant difference could be observed between the three subgroups about SE-S and μ_{raf1a}. A significant ($p<0.005$) difference could be observed between sBCC and the other two groups concerning DEJ-S, PDRJ-S, presence of NOD-L, μ_{raf2} and $\mu_{raf3a,}$. A significant difference ($p<0.001$) in E-T, PD-T and P&F-L3, μ_{raf1b} and μ_{raf3b} could be detected between the three subgroups.

#260406 Received 2 Mar 2016; revised 15 May 2016; accepted 15 May 2016; published 19 May 2016

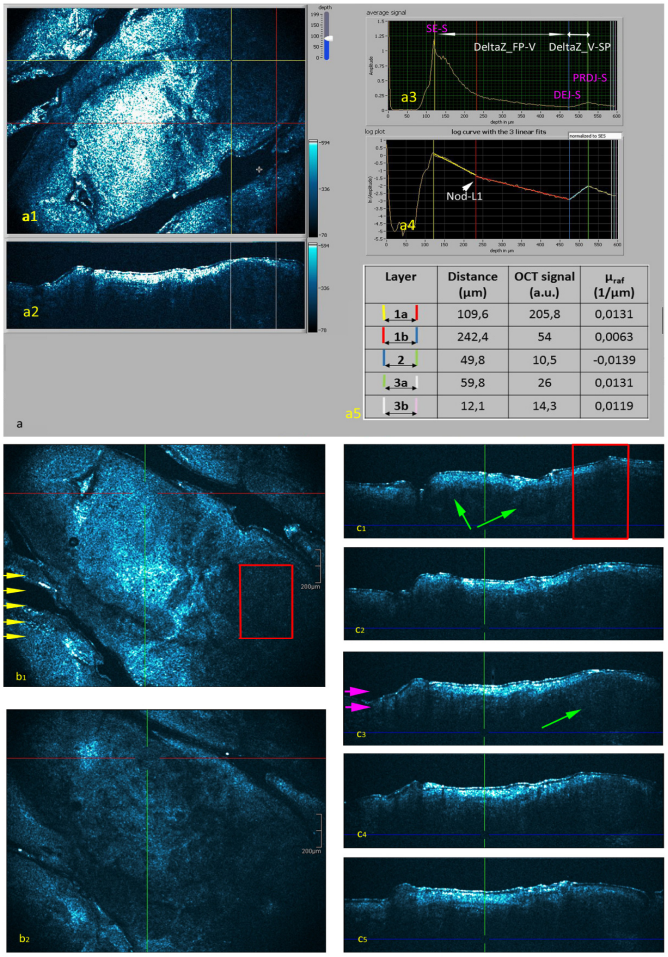

Fig. 1. Superficial BCC. (a) A 3-D HD-OCT DICOM (digital imaging and communication in medicine) image of the lesion is selected: en face image (a1) and cross-sectional image (a2). This DICOM file is then opened using LabView software. A region of interest (ROI) (> 0.1 mm^2) is chosen in the en face image (red square). In a first step, a plot z-axis profile of the scanned volume (> 0.05 mm^3) is performed. The obtained graph (a3) displays the reflectance and attenuation of the ballistic photons (OCT-signal: measured on the y-axis with arbitral units (a.u.)) versus imaging depth which is indicated on the x-axis (µm). The distance from Z = 0 to the first peak is the thickness of the gel. The first peak at about 120 µm corresponds to the skin entrance signal (SE-S). The valley is noticed 352 µm deeper than the first peak. Consequently, the epidermis is approximately 232 µm thick in this ROI. The second peak is situated 50 µm deeper than the valley. Hence, the papillary dermis is approximately 50 µm thick in this ROI. In a second step, The HD-OCT signals were divided by SE-S in order to normalize them to the SE-S The natural logarithm ln(x) of those values is taken (a4). A semi-log plot is performed; an exponential function becomes linear described by y = ax + b. Successive layers with clear exponential decay are identified and plotted. A straight line is fitted in each of these layers resulting in equation of type yi = axi + b whereby coefficient a provides the relative attenuation factor for each of the identified layers "i" given by μ_{rafi}. Data are summarized in table (a5): OCT signal at different Z-values (a.u.), distance (µm) between different Z values (vertical coloured lines) and μ_{raf} in different layers (1/µm). (b) high-resolution en face images at different Z-values. Yellow arrows indicate the position of cross-sectional images (c). Magenta arrows indicate the position of the en face images. Green arrows indicate the sBCC hemi-lobules. **Optical properties of sBCC** with high diagnostic accuracy (>95%) and high negative predictive values (NPV) (>97.5%) are the presence of a nod in semi-log plot of layer-1, much lower relative attenuation factor in lower part of epidermal layer (μ_{raf1b}) and strongly increased E-T.

#260406 Received 2 Mar 2016; revised 15 May 2016; accepted 15 May 2016; published 19 May 2016

Table 2. Quantitative evaluation of relevant parameters observed in basal cell carcinoma subtypes in comparison with normal adjacent skin.

OPTICAL PROPERTIES	**sBCC**	**NL-sBCC** Trunk 16/16	**Δ** sBCC versus NL-sBCC	**nBCC**	**NL-nBCC** Face 15/16 Trunk 1/16	**Δ** nBCC versus NL-nBCC	**iBCC**	**NL-iBCC** Face 14/16 Trunk 2/16	**Δ** iBCC versus NL-iBCC
SE-S (a.u.)	465.87 [+/-87.66] **NS**	362.93 [+/- 66.25] **(p<0.01)**	**p<0.001**	552.72 [+/-121.69] **NS**	539.19 [+/- 111] **NS**	**NS**	578.40 [+/-104.00] **NS**	549.57 [+/- 68.32] **NS**	**NS**
DEJ-S (a.u.)	50.98 [+/- 16.89] **(p<0.001)**	97.61 [+/- 19.87] **NS**	**p<0.001**	256.12 [+/- 77.91] **NS**	179.17 [+/- 100.33] **NS**	**NS**	186.40 [+/- 22.30] **NS**	132.48 [+/- 18.95] **NS**	**p<0.001**
PRDJ-S (a.u.)	73.86 [+/- 19.13] **(p<0.001)**	143.6 [+/- 35.61] **(p<0.01)**	**p<0.001**	367.49 [+/-93.77] **NS**	289.36 [+/-61.68] **NS**	**NS**	357.93 [+/- 78.62] **NS**	266.81 [+/- 44.89] **NS**	**p<0.01**
E-T (μm)	188.25 [+/-39.12] **(p<0.001)**	84.61 [+/- 9.96] **(p<0.01)**	**p<0.001**	25.81 [+/-4.29] **(p<0.001)**	54.38 [+/- 8.99] **NS**	**p<0.0001**	43.25 [+/-7.59] **(p<0.001)**	63.60 [+/- 7.12] **NS**	**p<0.0001**
PD-T (μm)	49.81 [+/-7.85] **(p<0.001)**	42.49 [+/- 6.74] **(p<0.01)**	**NS**	16.87 [+/-2.52] **(p<0.0001)**	25.53 [+/- 4.44] **NS**	**p<0.001**	25.62 [+/-1.62] **(p<0.001)**	33.26 [+/-5.91] **NS**	**p<0.01**
NOD-L1	16/16 **(p<0.001)**	16/16 **NS**	**NS**	0/16 **NS**	16/16 **NS**	**P<0.001**	0/16 **NS**	16/16 **NS**	**p<0.001**
NOD-L3	16/16 **NS**	16/16 **NS**	**NS**	16/16 **NS**	16/16 **NS**	**NS**	16/16 **NS**	16/16 **NS**	**NS**
P&F-$L3_{am}$ ($\sum$ of $\sum$ per lesion) / 16	0.25 [+/- 0.28] **(p<0.001)**	0.68 [+/- 0.37] **NS**	**NS**	1.43 [+/- 0.61] **(p<0.001)**	0.31 [+/- 0.26] **NS**	**p<0.01**	2.87 [+/-0.73] **(p<0.001)**	0.31 [+/- 0.26] **NS**	**p<0.0001**
μ_{raf1a} (μm^{-1})	0.02781 [+/-0.0098] **NS**	0.02692 [+/- 0.0069] **(p<0.01)**	**NS**	0.0410 [+/-0.0098] **NS**	0.0579 [+/- 0.0117] **NS**	**P<0.01**	0.0265 [+/-0.0053] **NS**	0.0461 [+/-0.0090] **NS**	**p<0.01**
μ_{raf1b} (μm^{-1})	0.0101 [+/-0.0015] **(p<0.001)**	0.0146 [+/- 0.0008] **NS**	**p<0.001**	0.0410 [+/-0.0098] **(p<0.001)**	0.0156 [+/- 0.0052] **NS**	**p<0.001**	0.0265 [+/-0.0053] **(p<0.001)**	0.0180 [+/-0.0031] **NS**	**p<0.01**
μ_{raf2} (μm^{-1})	-0.0114 [+/- 0.0029] **(p<0.005)**	-0.0119 [+/- 0.0032] **(p<0.01)**	**NS**	-0.0226 [+/- 0.0079] **NS**	-0.0468 [+/- 0.0107] **NS**	**P<0.01**	-0.0380 [+/- 0.0097] **NS**	-0.0393 [+/- 0.0118] **NS**	**NS**
μ_{raf3a} (μm^{-1})	0.0135 [+/-0.0017] **(p<0.001)**	0.0153 [+/- 0.0032] **(p<0.01)**	**NS**	0.0360 [+/-0.0128] NS	0.0243 [+/- 0.0030] **NS**	**NS**	0.0235 [+/-0.0044] **NS**	0.0266 [+/-0.0049] **NS**	**NS**
μ_{raf3b} (μm^{-1})	0.0119 [+/-0.0017] **(p<0.001)**	0.0147 [+/- 0.0024] **(p<0.01)**	**NS**	0.0076 [+/- 0.0009] **(p<0.001)**	0.0067 [+/- 0.0002] **(p<0.01)**	**NS**	0.0229 [+/- 0.0044] (p**<0.001**)	0.0121 [+/- 0.0021] **(p<0.01)**	**p<0.01**

Values given are mean values and 95% confidence interval. **The p-values (in bold)** in ***columns 2, 5 and 8***: tested p-values between the respective BCC subtypes; in ***columns 3, 6 and 9***: tested p-values between the respective adjacent normal skins of sBCC, nBCC and iBCC; in ***columns 4, 7 and 10***: tested p-values of difference between each BCC subtype and their respective adjacent normal skin. **NS:** not significant.

3.3 Selection of best critical value of IV-OP

Critical values permitting differentiation of the three subgroups could be defined by applying the ROC curves (Table 3).

#260406 Received 2 Mar 2016; revised 15 May 2016; accepted 15 May 2016; published 19 May 2016

Table 3. Selection of best critical value of relevant optical properties of basal cell carcinoma subtypes by applying receiver operating characteristic curves.

Optical properties	Critical value	Area under ROC curve	Sensitivity	Specificity	Accuracy	Positive likelihood ratio
DIFFERENTIATING SUPERFICIAL BCC FROM OTHER SUBTYPES						
E-T (µm)	>69	0.998	100%	96.87%	97.9%	32
Presence NOD-L1	Yes	1	100%	100%	100%	
Relative attenuation factor layer1b (μm^{-1})	<0.0172	0.928	100%	87%	91.7%	8
DIFFERENTIATING NODULAR BCC FROM OTHER SUBTYPES						
PD-T (µm)	< 23	0.981	93.8%	96.9%	95.83%	15
Less negative μ_{raf2} compared to normal skin (μm^{-1})*	Increase >0.0147	0.940	87.5%	93.8%	91.7%	9.3
DIFFERENTIATING INFILTRATIVE BCC FROM OTHER SUBTYPES						
Peaks&Falls-L3 (mean)	>1	0.861	87.5%	75%	79.17%	3.5
Increased μ_{raf3b} (μm^{-1}) compared to normal skin°	>0.0051	0.940	93.8%	93.8%	93.8%	13
* Δ nBCC- NL-nBCC: 0.024 μm^{-1} [+/– 0.0081] ($p<0.01$) compared to other subgroups.						
° Δ iBCC- NL-iBCC: 0.0114 μm^{-1} [+/– 0.0045] ($p<0.01$) compared to other subgroups.						

3.4 Absolute and relative frequencies of IV-OP in relation to best critical values (Table 4)

3.4.1 Differentiation of sBCC from other BCC subtypes (Fig. 1)

E-T >69 µm was highly sensitive and specific for sBCC (100% and 96.87% respectively; NPV = 100%, PPV = 94.1%, $\phi = 0.95$ and $X^2 = 43.76$, $p<0.0001$). The diagnostic accuracy was 97.9%. Nod-L1 was a very highly sensitive and specific feature for sBCC (both 100%). No nod in layer-1 could be observed in other BCC subtypes. The μ_{raf1b} <0.0172 cm^{-1} was highly sensitive and moderately specific for sBCC (100% and 87% respectively; NPV = 100%, PPV = 80%, $\phi = 0.84$ and $X^2 = 33.6$, $p<0.0001$). The diagnostic accuracy was 91.7%.

3.4.2 Differentiation of nBCC from other BCC subtypes (Fig. 2)

PD-T <23 µm was highly sensitive and specific for nBCC (93.8% and 96.9% respectively; NPV = 96.88%, PPV = 93.75%, $\phi = 0.91$ and $X^2 = 39.42$, $p<0.0001$). The diagnostic accuracy was 95.83%. A less negative μ_{raf2} (increase of > 0.0147 cm^{-1}) compared to normal skin was highly sensitive and specific for nBCC (85.7% and 93.8% respectively; NPV = 93.8%, PPV = 87.5%, $\phi = 0.81$ and $X^2 = 31.69$, $p<0.001$). The diagnostic accuracy was 91.7%.

3.4.3 Differentiation of iBCC from other BCC subtypes (Fig. 3)

P&F-L3 was moderately sensitive and modestly specific for iBCC (87.5% and 75% respectively; NPV = 92.31%, PPV = 63.64%, $\phi = 0.59$ and $X^2 = 16.78$, $p<0.0001$). The diagnostic accuracy was 79.17%. An increase of μ_{raf3b} of >0.0051 cm^{-1} compared to normal skin was highly sensitive and specific for iBCC (both 93.8%; NPV = 96.8%, PPV = 88.2%, $\phi = 0.86$, $X^2 = 35.7$, $p<0.001$). The diagnostic accuracy was 93.8%.

#260406 Received 2 Mar 2016; revised 15 May 2016; accepted 15 May 2016; published 19 May 2016

4. Discussion

The non-invasive diagnosis of BCC and its clinical/pathological sub-differentiation has recently become of great importance for the correct management of the disease [36]. With the emergence of non-invasive therapy for sBCC there is an urgent demand for non-invasive diagnosis.

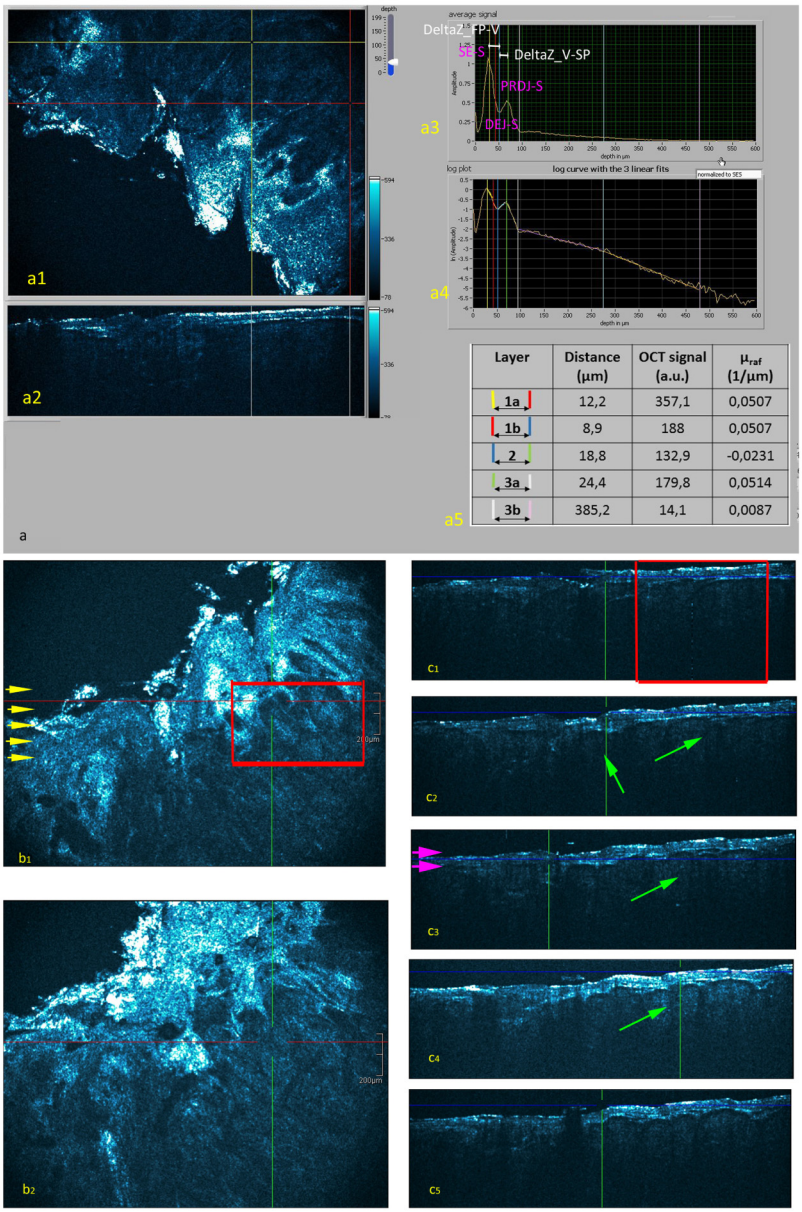

Fig. 2. Nodular BCC. (a-c). For details about arrows see Fig. 1. Optical properties of nBCC with moderate to high diagnostic accuracy (91.7% - 95.8%) and high NPV (93.8% - 97.0%) were strongly decreased epidermal - and papillary dermal thickness and less negative µraf2 compared to normal skin.

Two major problems occur with non-invasive imaging technologies in BCC. First, the diagnostic performance of these techniques varies with the user's experience and would be

#260406 Received 2 Mar 2016; revised 15 May 2016; accepted 15 May 2016; published 19 May 2016

consequently poor for non-expert physicians. The second problem is related to their limited capability to differentiate BCC subtypes. The results of a previous study by our group [33] were in line with literature data approaching the same problem with other methodologies [20]. Indeed, the distinction of BCC subtypes by means of reflectance confocal microscopy is mainly based on the assessment of BCC tumour islands (presence of palisading) thanks to the higher resolution of that technique as compared to HD-OCT [20]. Conversely, the discrimination of BCC subtypes by means of dermoscopy is mainly based on the vascular pattern [13–15] along with the presence of large blue-grey ovoid nests [15]. HD-OCT approach needs to combine both tumour islands assessment and vessel organization, to reach a good discrimination between different BCC subtypes, with the added advantage to explore the skin in depth (up to 570 µm) [15]. This comprehensive examination of the skin in depth is crucial, as it allows the visualisation of stretching effect that the tumour islands exert on the stroma, a feature that was detected in 95% of nBCC and 100% of iBCC, but in none of the sBCCs of our previous series [33].

Table 4. Absolute and relative frequencies of relevant optical properties of BCC subtypes in relation to critical values as assessed in vivo by High-Definition Optical Coherence Tomography

	SUPERFICAL BCC N = 16	NODULAR BCC N = 16	INFILTRATIVE BCC N = 16
DIFFERENTIATING SUPERFICIAL BCC			
E-T > 69 µm	16 (100%) **(p<0.0001)**	0 (0%)	1 (6.25%)
Presence of nod in layer1 (Yes)	16 (100%) **(p<0.0001)**	0 (0%)	0 (0%)
Relative attenuation factor layer1b < 0.0172 (μm^{-1})	16 (100%) **(p<0.0001)**	1 (6.25%)	3 (18.75%)
DIFFERENTIATING NODULAR BCC			
PD-T < 23 µm	0 (0%)	15 (93.75%) **(p<0.0001)**	1 (6.25%)
Less negative μ_{raf2} compared to normal skin: increase with > 0.0147 μm^{-1}	1 (6.25%)	14 (87.5%) **(p<0.001)**	1 (6.25%)
DIFFERENTIATING INFILTRATIVE BCC			
Supplementary peaks &falls in superficial reticular dermis >1	1 (6.25%)	7 (43.75%)	14 (87.5%) **(p<0.001)**
> 0.0051 μm^{-1} increase of μ_{raf3b} compared to normal skin	0 (0%)	2 (12.5%)	14 (87.5%) **(p<0.001)**
*p-values have been added whenever appropriate; for details see result section			

Both problems could be tackled by the introduction of user-independent automated classification systems of skin lesions based on their optical properties, which could be achieved by other techniques, such as spectrophotometric technologies [35]. Recent developments in this field concerning the diagnosis of BCC include imaging modalities such as elastic scattering spectroscopy and spectrophotometric intra-cutaneous analysis [36].

HD-OCT permitted also the assessment of in vivo optical properties such as light attenuation in intrinsic ageing skin [38] and in melanocytic lesions [39]. This approach seems to permit a semi-automated classification of lesions which is easier to handle by non-experts. The technique of semi-log plot whereby an exponential function becomes linear described by $y = ax + b$ has been implemented on HD-OCT signals coming from three successive skin layers (epidermis, papillary dermis and superficial reticular dermis). This permitted the in vivo measurement of OCT signals at specific imaging depth such as SE, DEJ and PRDJ. To measure an absolute attenuation coefficient it is necessary to a have a measurement system with a perfectly linear behavior. This was however not tested to the full extent with the used Skintell. The best compromise was to use the skin entrance signal as reference as this signal

#260406 Received 2 Mar 2016; revised 15 May 2016; accepted 15 May 2016; published 19 May 2016

is clearly defined. Moreover, absolute values of the attenuation are not required as only differences were taken into account. The relative attenuation factor (μ_{raf}), which is the attenuation coefficient normalized to skin entrance signal, was assessed in epidermis, papillary dermis and superficial reticular dermis. HD-OCT operates in the second diagnostic window of the NIR spectrum [38,39] and hence the main attenuation mechanism for HD-OCT is scattering. It can be assumed therefore that μ_{raf} is proportional to the reduced scattering coefficient. The presence/absence of Nod-L1, Nod-L3 and P&F-L3 could be observed.

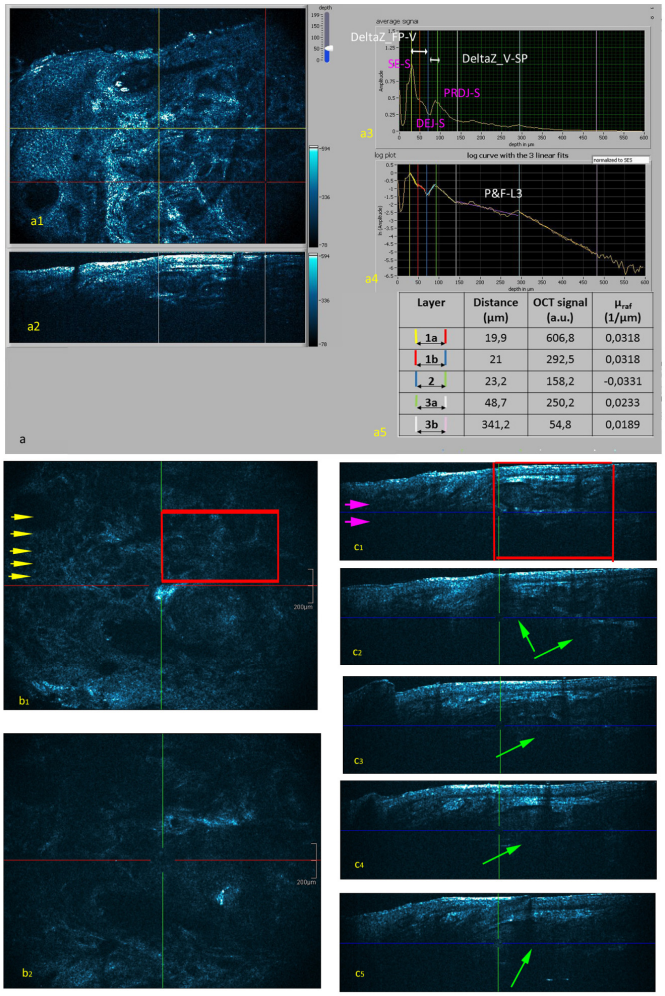

Layer	Distance (µm)	OCT signal (a.u.)	μ_{raf} (1/µm)
1a	19,9	606,8	0,0318
1b	21	292,5	0,0318
2	23,2	158,2	-0,0331
3a	48,7	250,2	0,0233
3b	341,2	54,8	0,0189

Fig. 3. Infiltrative BCC. (a-c) For details see Fig. 1. Regarding the optical properties of iBCC an increase of µraf3b of >0.0051 cm^{-1} compared to normal skin and the presence of peaks and falls in reticular dermis had good diagnostic accuracy (79.1% - 93.8%) and high NPV (93.8% - 96.8%).

Because the optical properties of human skin can vary significantly between individuals with different race, age and sun exposure, it is important to consider the difference in optical properties between lesioned skin and surrounding healthy skin region [44]. Critical optical properties were selected in a first step based on presence of significant differences between normal and lesioned skin. In a second step the differences regarding these properties among BCC subtypes were analyzed.

#260406 Received 2 Mar 2016; revised 15 May 2016; accepted 15 May 2016; published 19 May 2016

The sBCCs seems to be mainly located on the trunk where the UV-induced skin damage is less pronounced compared to the predominant facial localization of nBCCs and iBCCs, which are characterized by more intense sun-damage [15]. Intrinsic age and skin layer related values of μ_{raf} are displayed in Table 5 (unpublished data). The μ_{raf1} in normal aged skin was in line with μ_{raf1a} of normal skin adjacent to BCC observed in this study. In papillary dermis of normal aged skin NIR light is backscattered even when solar elastosis is absent (μ_{raf2} has a negative value). In normal skin adjacent to nBCC and iBCC light at papillary dermis is even more backscattered compared to intrinsic aged skin probably by the presence of solar elastosis. In the normal reticular dermis a Nod-L3 is observed dividing this layer in a superficial and deeper part. Normal μ_{raf3a} is not significant different according to age or anatomic site. However μ_{raf3b} decreases significantly with ageing suggesting an intrinsic ageing related increase in anisotropy of scattering in lower layers.

A highly significant difference between BCC subtypes could be observed with regard to the measured optical properties. From a clinical point of view, it is more disastrous if iBCC is misdiagnosed as sBCC then if a sBCC is mistaken for an iBCC [5]. Hence decision criteria minimizing the false negative rate deserve priority. Therefore critical values could be determined for these optical properties permitting differentiation of sBCC from more aggressive BCC lesions with high area under the ROC curve and high positive likelihood ratio's.

Optical properties of sBCC with high diagnostic accuracy (>95%) and high NPV (>97.5%) were (i) significant lower μ_{raf1b}. and (ii) strongly increased epidermal thickness. These findings were the optical correlates of hemispherical grey to dark structures connected to the epidermis and resembling swallow nests. These are one of the morphological HD-OCT features diagnostic for sBCC [15]. The other typical feature is the presence of short fine holes spiral-shaped winded, localized around a central focus near the DEJ. The epidermis in sBCC was much thicker. The presence of Nod-L1 and subsequently different μ_{raf1a} and μ_{raf1b} values corresponded most probably to a change in size of scatterers in the swallow nests connected to the epidermis (see further). Compared to normal adjacent skin no significant differences could be found regarding the other μ_{raf}. All sBCC were located on the trunk.

Although HD-OCT imaging missed deeper located (>570 µm) parts of the iBCC and nBCC, some significant differences of optical properties between these subtypes could be observed in comparison with normal adjacent skin.

Optical properties of nBCC with moderate to high diagnostic accuracy (91.7% - >95.8%) and high NPV (93.8% - 97%) were (i) less negative μ_{raf2} values compared to normal adjacent skin, and (ii) strongly decreased epidermal and papillary dermal thickness. These optical characteristics were in line with the morphological HD-OCT findings in nBCC [33]. These features are the presence of lobular structures with bright outer rim (cockade feature) located in the upper dermis. The roof of these lobules was observed at Z-values less than 75 µm from the skin surface. Moreover small branched holes are embedded in the outer bright rim. This explains the observed significant lesser negative μ_{raf2} values, compared to normal adjacent skin. The papillary dermis in between the epidermis and lobular structures was squeezed resulting in strongly decreased papillary dermal thickness. The epidermis in nBCC was remarkably thin explaining the very low epidermal thickness. The μ_{raf3a} and μ_{raf3b} did not differ significantly from normal adjacent skin. Almost all nBCC in this study were located on the face.

Regarding the ***optical properties of iBCC*** both the increase of μ_{raf3b} of >0.0051 cm^{-1} compared to normal skin and the presence of peaks and falls in reticular dermis had high diagnostic accuracy (79.1% - 93.8%) and high NPV (93.8% - 96.8%). This was in line with the morphological HD-OCT findings in iBCC [33] which are lobulated structures into the deeper dermis. The roof of these structures is noticed at Z-values more than 150-µm from skin surface [33]. Large branched holes are embedded in a distorted fibrous stroma. There is a pronounced distortion of fibrous structures aligned in one direction and localized in

#260406 Received 2 Mar 2016; revised 15 May 2016; accepted 15 May 2016; published 19 May 2016

between the lobules (stretching effect). These explained the significantly higher μ_{raf3b} compared to normal adjacent skin and the presence of supplementary P&F-L3; peaks (increased NIR light backscattering) followed by falls (increased NIR light attenuation) corresponding with the grey core of the lobulated structures. The μ_{raf3} remained high with depth in iBCC compared to normal skin; a finding that was absent in nBCC. These findings are in line with previous observations [54]. The OCT signal at DEJ and PRDJ was significantly increased in iBCC compared to normal adjacent skin. This was also observed in nBCC although the higher values in nBCC contrasted not significantly with those observed in adjacent normal skin.

Optical property measurements sensitive for scattering and anisotropy factor ***g*** offer the best means of characterizing the micro-architecture of cells and tissues [43]. A decrease in μ_{raf} implies an increase in anisotropy factor g [43]. Hence, a decrease of μ_{raf1b} in sBCC implied an increase in size of scatterers and consequently an increase in anisotropy factor g at the lower epidermal levels and in the swallow nests of this subtype. High g values in layer-1b (> 0.9) corresponding with strong anisotropic scattering, seemed to be characteristic for sBCC. Forward scattering became more likely. Hence the lower epidermis became much more translucent compared to the other BCC subtypes. Both nBCC and iBCC are characterized by higher μ_{raf1} and consequently lower g values (< 0.8), which correspond to more isotropic scattering.

Table 5. Intrinsic age and skin layer related values of relative attenuation factors. Measurements are taken at inner site of right upper arm.

Relative attenuation factor	Pre-menopausal women	Post-menopausal women
layer1 (μm^{-1})	0.0098 [+/– 0.0012]	0.0375 [+/– 0.0037]
layer2 (μm^{-1})	–0.0138 [+/– –0.0026]	–0.0197 [+/– –0.0038]
Layer3a* (μm^{-1})	0.0241 [+/–0.0039]	0.0271 [+/–0.0051]
Layer3b* (μm^{-1})	0.0150 [+/–0.0023]	0.0075 [+/– 0.0009]
(*) nod in semi-log plot is present in layer 3: "3a" upper part and "3b" lower part		

Some major limitations of this study need to be mentioned. The main limitation of HD-OCT for BCC diagnosis is the limited penetration depth. The second limitation is the selection bias at several levels: i) selection of the lesions for the study conditioned by the availability of "good quality" HD-OCT images, ii) selection of the tumor area sampled because lesions are usually much larger than HD-OCT field of view (1.5x1.8mm), and iii) the appropriate selection of the skin volume in a DICOM image for IV-OP analysis which requires experience with HD-OCT. These facts questions to some extent the accuracy of HD-OCT in the hands of non-experts. The method called OCT based tissue injury mapping [55] could be useful for selection of regions of interest based on structural an microvascular information. As this study only represents a training set, further validation studies need to be performed. The third issue is related to transitions between the three mentioned BCC categories, which are not rare. In this study we deliberately focused on histological proven clear-cut BCC subtypes. A fourth problem is linked to potential imitators of basal cell carcinoma. As a first step it was decided to concentrate on BCC alone.

In conclusion, HD-OCT seems to enable the rather unique combination of in vivo morphological analysis of cellular and micro-architectural structures with in vivo analysis of optical properties of tissue scatterers. In vivo HD-OCT analysis of optical properties permits BCC sub-differentiation with higher accuracy than in vivo HD-OCT analysis of morphology alone. The diagnostic performance of HD-OCT in BCC should be further assessed in other, multicenter clinical settings combining both types of analysis.

Acknowledgment

We are grateful to Rainer Nebosis (Dsc) and Frans Dhaenens (MD) of the research department of Agfa HealthCare for their help in accomplishing this study.

#260406 Received 2 Mar 2016; revised 15 May 2016; accepted 15 May 2016; published 19 May 2016